nature biotechnology

Quantitative fluorescence imaging of protein diffusion and interaction in living cells

Jérémie Capoulade[1,3], Malte Wachsmuth[1,3], Lars Hufnagel[1] & Michael Knop[1,2]

Diffusion processes and local dynamic equilibria inside cells lead to nonuniform spatial distributions of molecules, which are essential for processes such as nuclear organization and signaling in cell division, differentiation and migration[1]. To understand these mechanisms, spatially resolved quantitative measurements of protein abundance, mobilities and interactions are needed, but current methods have limited capabilities to study dynamic parameters. Here we describe a microscope based on light-sheet illumination[2] that allows massively parallel fluorescence correlation spectroscopy (FCS)[3] measurements and use it to visualize the diffusion and interactions of proteins in mammalian cells and in isolated fly tissue. Imaging the mobility of heterochromatin protein HP1α (ref. 4) in cell nuclei we could provide high-resolution diffusion maps that reveal euchromatin areas with heterochromatin-like HP1α-chromatin interactions. We expect that FCS imaging will become a useful method for the precise characterization of cellular reaction-diffusion processes.

Determining the properties of biomolecules—particularly of proteins—in their natural environment is a critical step in analyzing their functions and elucidating the mechanisms behind cellular and developmental processes. Analysis of local concentration fluctuations by FCS[3] provides information about mobile and immobile fractions of labeled molecules, their diffusion properties and absolute concentrations, as well as the co-diffusion of differentially labeled molecules that interact with each other[5,6]. FCS measurements performed at single points in the sample using confocal microscopes enable quantification of the dynamics of protein complex formation involved in signaling (by us[7] and others[8]), the study of nuclear export–competent mRNA-protein particles[9], the dynamics of prion aggregation[10] or the characterization of morphogen gradients[11].

FCS experiments are technically demanding as they require many fluorescence fluctuations to be recorded per individual measurement (usually over periods of seconds to minutes). The geometry of a confocal setup leads to out-of-focus illumination, so that the associated photobleaching often permits only one or a few single-point measurements per cell at specifically selected positions[7,12]. Further complications arise from the heterogeneous interior of cells and from cellular movements.

Recently, FCS technology has been extended in several ways. Dual-focus and scanning confocal FCS have improved the accuracy of local diffusion measurements[11,13]. Image-correlation approaches[14] have provided spatially resolved data, albeit only with a resolution in the range of a few micrometers. Also, electron-multiplying charge-coupled device (EM-CCD) camera-based methods have been used to acquire FCS data in a parallelized manner. Using a selective plane illumination microscope (SPIM)[15] has enabled FCS imaging of fluorescent beads moving in the bloodstream of fish embryos[16]. Total internal reflection fluorescence microscopy has facilitated FCS imaging of protein diffusion at diffraction-limited resolution in the periphery of cells[17]. Spinning-disc or line-confocal microscopes have allowed multifocal FCS measurements of protein diffusion, however, only at foci distributed along a line or rather sparsely in two dimensions[18,19]. By contrast, we perform high-resolution FCS imaging of protein mobility with continuous and complete spatial and temporal coverage of two-dimensional (2D) sections inside living cells or tissue.

To achieve this, we needed to reduce photobleaching of the sample while retaining optical sectioning capabilities similar to those of confocal microscopy. The designed microscope setup consists of three major modules (**Fig. 1a** and **Supplementary Fig. 1**): an illumination unit that generates a laterally confined and thin diffraction-limited light-sheet (**Fig. 1a** (i)); a detection unit that contains a camera with single-molecule sensitivity to observe the focal region of the light-sheet referred to as the light-pad (**Fig. 1a** (ii)); and an inverted microscope that allows convenient positioning of specific areas of the specimen in the light-pad (**Fig. 1a** (iii)). The purpose of (i) and (ii) is to illuminate only the precise section of the cell that is in focus in the detection unit. This should improve parallelized FCS measurements compared to microscopes operated in epi-illumination mode.

The core of the optical setup consists of two orthogonally arranged identical 40×/0.8 numerical aperture (NA) long working-distance objective lenses that are dipped into a Petri dish containing the specimen. The illumination objective lens, conjugated to a cylindrical lens, generates the light-sheet, whereas the observation objective lens is used to collect the emitted fluorescence light. For intensity imaging, the light is directed to an imaging camera. For FCS imaging, an alternative light path is used for observation with a high-speed camera referred to as the FCS camera (**Fig. 1a**). An arrangement of two spatial filters, consisting of one slit in the illumination path and another one in the FCS imaging detection path, generates a rectangular image on the FCS camera that matches the light-pad.

The point spread function (PSF) of the microscope is nearly isotropic with a half-width at $1/e^2$ along the z axis of 410 nm centrally ($y = 0$) and

[1]Cell Biology and Biophysics Unit, European Molecular Biology Laboratory, Heidelberg, Germany. [2]Present address: Zentrum für Molekulare Biologie der Universität Heidelberg (ZMBH), DKFZ-ZMBH Allianz, Universität Heidelberg, Germany. [3]These authors contributed equally to this work. Correspondence should be addressed to M.W. (malte.wachsmuth@embl.de) or M.K. (m.knop@zmbh.uni-heidelberg.de).

835

Figure 1 FCS imaging using the diffraction-limited light-pad. (**a**) Front view of the main components of the light-pad microscope. The specimen is contained in a Petri dish. The first objective lens illuminates a thin slice in the specimen. Optical sectioning is performed under 45° with respect to the bottom of the Petri dish. The high aperture angle of the illumination light-sheet (74°) leads to weak illumination of cells lying outside the light-pad area (inset (i)). Fluorescence is detected at a right angle to the illumination plane by the detection lens. Spatial filters in the illumination path and the detection path confine the observed area to a rectangular array of volume elements, the light-pad (inset (ii)). An inverted microscope allows convenient positioning of the specimen. (**b**) Each individual pixel of the EM-CCD records a fluctuating fluorescence signal over time. These fluctuations are analyzed by temporal correlation analysis resulting in one ACF for each pixel. The ACF provides information about the diffusion coefficient D (dashed line) and the concentration C of diffusing fluorescently labeled molecules (amplitude of the curve).
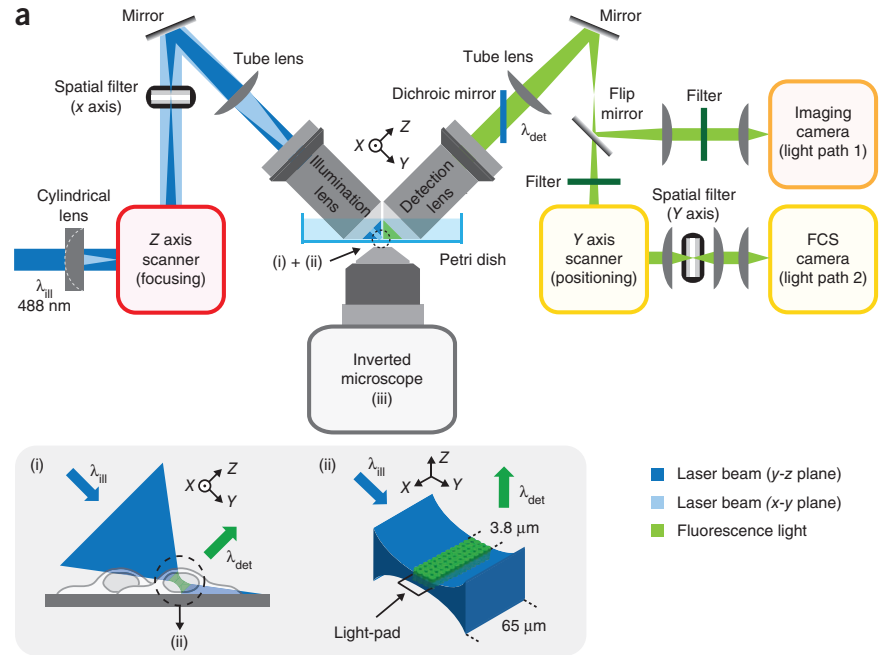
520 nm at the edge of the light-pad ($y = \pm 2\,\mu m$) and a half-width at $1/e^2$ in the xy plane of 370 nm (**Supplementary Results**, **Supplementary Fig. 2** and **Supplementary Video 1**). The chip of the used FCS camera subdivides the light-pad area of $3.8 \times 65\,\mu m^2$ into 20 lines of 340 pixels each. Every pixel of the FCS camera collects the light emitted from a corresponding observation volume element in the light-pad. Fluorescent molecules, such as GFP-tagged proteins, move in the sample, thereby crossing individual volume elements of the light-pad by diffusion or other modes of molecular motion. The resulting concentration fluctuations in each volume element are recorded in the form of fluorescence intensity fluctuations by the FCS camera (**Fig. 1b**), which provides single-photon sensitivity and high acquisition rates, from 25,000 lines/s for single-line acquisition (one dimensional (1D)-FCS) to 1,400 frames/s for 20 lines/frame acquisition (2D-FCS). Calculating temporal autocorrelation functions of the intensity traces and fitting them with an appropriate model (e.g., describing normal or anomalous diffusion) yields locally statistical information about frequency and speed of the movements of the fluorescent molecules, recorded at each pixel of the camera over the area of the light-pad (**Fig. 1b**).

Based on knowledge about the optical properties of the setup it is possible to calculate spatially resolved maps of protein concentrations and mobilities, especially maps of diffusion coefficients and interaction properties (Online Methods, **Supplementary Results**, **Supplementary Fig. 3** and **Supplementary Videos 2–4**).

To investigate the mobility of a fast diffusing fluorophore inside cells, we conducted FCS imaging of a 40 kDa fusion of the green-emitting monomeric Azami Green fluorescent protein with a fragment of human Geminin (mAG-hGem), a component of the cell cycle reporter system Fucci[20]. We used epithelial cells in the S/G_2 phase of the cell cycle where the protein is detected inside the nucleus (**Fig. 2a**). The 1D-FCS recordings (**Fig. 2b**) of cytoplasmic areas or extracellular space yielded only noncorrelated noise (**Fig. 2c**). By contrast, a diffusible pool was identified in the nucleus (**Fig. 2d**). Fitting these autocorrelation functions using a model function for anomalous diffusion for one component and applying corrections for medium-induced aberrations (equation (2) in Online Methods, **Supplementary Figs. 4** and **5**) resulted in an average apparent diffusion coefficient of $25 \pm 7\,\mu m^2\,s^{-1}$ (mean ± s.d.) and a concentration
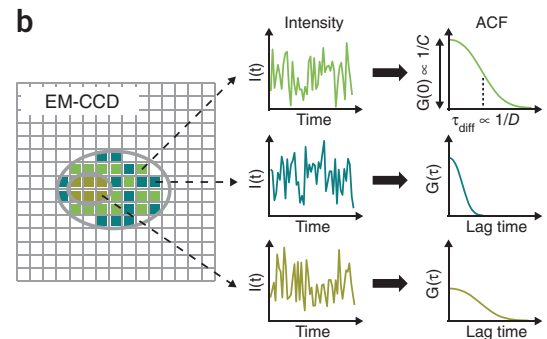
of the protein for this specific cell of 420 ± 120 nM (**Fig. 2e**). Independent validation of the diffusion coefficient was obtained by confocal FCS measurements ($24 \pm 10\,\mu m^2\,s^{-1}$; **Supplementary Fig. 6** and **Supplementary Table 1**). When we conducted 2D-FCS recordings of a 15×102 pixel area corresponding to $\sim 3 \times 19\,\mu m^2$ across a cell nucleus, we found a homogenous distribution of diffusion coefficients and concentrations, as expected for a protein that does not interact with cellular structures at this stage of the cell cycle (**Fig. 2f–k** and **Supplementary Fig. 5**). These data demonstrate that 1D- and 2D-FCS recordings using our microscope permit the measurement of diffusion coefficients of genetically encoded fluorescent proteins in living cells.

Many processes in tissue differentiation or embryogenesis involve reaction-diffusion–based mechanisms for signal propagation, for example by gradient-forming morphogens or hormone regulation[1,21]. Because FCS imaging would be an ideal method to study such processes, we tested whether our system can record data of sufficient quality from cells that are often small and buried in tissues with heterogeneous optical properties. To assess the feasibility of *in situ* measurements, we investigated the diffusion of nuclear localization signal (NLS)-GFP in isolated wing imaginal discs of *Drosophila melanogaster* larvae.

We first generated a three-dimensional (3D) reconstruction of a large area of a wing imaginal disc by scanning with the light-pad. This revealed detailed cellular structures up to a depth of $\sim 50\,\mu m$ (**Fig. 3a** and **Supplementary Video 5**). 2D-FCS imaging performed in selected areas of the wing discs provided a diffusion coefficient of NLS-GFP ($19 \pm 6\,\mu m^2\,s^{-1}$) inside cell nuclei up to $\sim 30\,\mu m$ inside

Figure 2 1D- and 2D-FCS imaging of protein diffusion in Madin-Darby canine kidney (MDCK) cells. (**a**) MDCK cells expressing a small green fluorescent protein fusion (mAG-hGem). The bright areas are nuclei where mAG-hGem is enriched. The dashed line indicates the position of the 1D-FCS recording. Scale bar, 10 μm. (**b**) Kymograph of the first 12 ms of the fluorescence signal acquired along the line in **a**. (**c**) Autocorrelation functions (ACFs) calculated from pixels outside the cells (region 1 in **b**). (**d**) ACFs calculated from pixels within a cell (region 2 in **b**). (**e**) Profiles of intensities, concentrations and apparent diffusion coefficients of mAG-hGem obtained from fitting the ACFs to a one-component model for anomalous diffusion. The intensity profile (gray line) represents the averaged intensity of the first 500 ms of the acquired data. (**f**) mAG-hGem MDCK cell selected for 2D-FCS recording. The dashed rectangle indicates the area of the 2D-FCS recording corresponding to the light-pad. Scale bar, 10 μm. (**g**) First five frames of the recorded data. (**h**) ACFs calculated for the nuclear region highlighted in **g** with a dashed rectangle. (**i**) Intensity map of the area used for 2D-FCS imaging (averaged over the first 500 ms of the acquired data). The dashed rectangle highlights the same region as in **g** where the ACFs shown in **h** were extracted. Scale bar, 2.5 μm. (**j**) Map of the concentrations of mAG-hGem obtained from fitting the ACFs to a one-component model for anomalous diffusion. (**k**) Map of the apparent diffusion coefficients of mAG-hGem obtained from the same model fitting. Time resolution, 70 μs (1D-FCS) and 700 μs (2D-FCS).
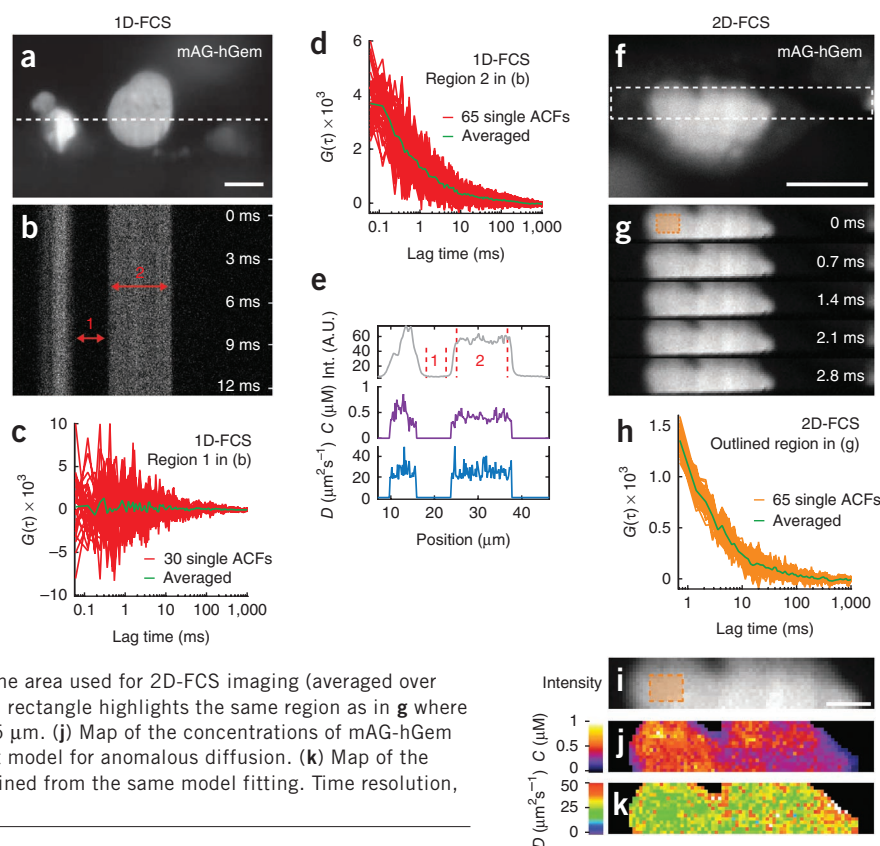

the tissue (**Fig. 3b–e** and **Supplementary Figs. 5** and **7**). The measured values were fully consistent with confocal FCS (14 ± 2 μm^2 s^{-1}, **Supplementary Fig. 6** and **Supplementary Table 1**). This demonstrates the suitability of the microscope for studying the diffusion of GFP-labeled proteins inside embryonic tissue samples.

To explore the applicability of FCS imaging to study the spatial distributions of protein dynamics, we investigated the interactions of the α isoform of heterochromatin protein 1 (HP1α) with chromatin. This protein mainly binds to methylated nucleosomes, but also to other chromatin-binding and chromatin-forming proteins[22,23]. Because the HP1 family of proteins has important roles in transcriptional repression, heterochromatin establishment, maintenance and euchromatin organization[24,25], the dynamics of their interactions with chromatin has been studied in detail. Photobleaching and confocal FCS revealed

highly dynamic GFP-HP1α interactions in all chromatin domains[4,26]. These observations led to the conclusion that diffusion-controlled processes underlie heterochromatin organization[4].

In confocal FCS, the interaction of HP1α with chromatin was identified as the slowly diffusing component of a two-component fit of the autocorrelation functions. In pericentric heterochromatin, identified as small regions with high GFP-HP1α signal (**Fig. 4a,b**), the measured values of the apparent diffusion coefficient of the slow component were in the range of 0.07–0.25 μm^2 s^{-1}. For euchromatin, we obtained values for this component in the range of 0.16–0.65 μm^2 s^{-1}. The distribution of values from both chromatin domains revealed a considerable overlap (**Fig. 4c**). It was not possible to interpret the origin of these distributions, which may result from experimental errors associated with individual measurements, or may reflect genuine differences

Figure 3 2D-FCS imaging of protein diffusion in *Drosophila* wing imaginal discs. (**a**) Optical sections of a wing imaginal disc from a *Drosophila* larva expressing GFP-NLS (single section stitched from four adjacent images) imaged with the light-pad microscope. To obtain these images, the numerical aperture of the illumination was reduced to increase the focal depth of the light-sheet. Two sections at a distance of 45 μm are shown (a 3D reconstruction of the full stack is provided with **Supplementary Video 5**); scale bar, 10 μm. (**b**) Intensity map of an area of a wing disc used for 2D-FCS imaging (averaged over the first 500 ms of the acquired data). Scale bar, 5 μm. (**c**) Autocorrelation functions (ACFs) calculated for the region delimited by dashed lines in **b**. (**d,e**) Maps of the concentrations (**d**) and of the apparent diffusion coefficients (**e**) of GFP-NLS, obtained from fitting the ACFs to a one-component model for anomalous diffusion. 2D-FCS time resolution, 700 μs.
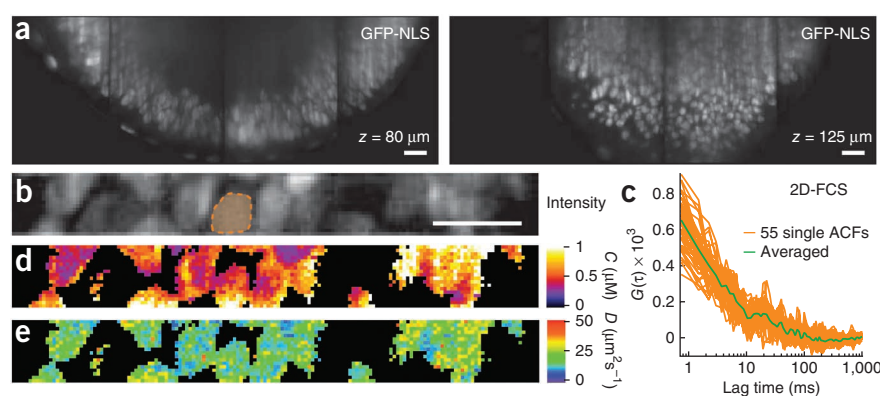
Figure 4 Spatially resolved HP1α mobility in 3T3 cells investigated by 2D-FCS imaging. (**a**) 3T3 cell expressing HP1α-EGFP. The arrowheads mark the positions (gray, cytoplasm; purple, euchromatin; green, heterochromatin) where the autocorrelation functions (ACFs) from confocal FCS measurements shown in **b** were acquired. Euc.: euchromatin; Heteroc.: heterochromatin. Scale bar, 10 μm. (**c**) Scatter plots of the diffusion coefficient D of HP1α in heterochromatin and euchromatin (slow component), resulting from confocal FCS measurements in six cells. The gray band highlights the overlap of the diffusion coefficient of eu- and heterochromatin. (**d**) Light-pad intensity image of the part of a 3T3 cell expressing HP1α-EGFP used for FCS imaging (overview image shown in **Supplementary Fig. 8a**). The light-pad crosses nuclear (bright area) and cytoplasmic regions (very dim areas around the nucleus) for this cell. (**e**) Map of apparent diffusion coefficients of HP1α-EGFP (slow component) obtained from fitting the ACFs to a two-component anomalous diffusion model. (**f**) The color-coded diffusion coefficient map (**e**) was intensity weighted with the inverted intensity image (**d**) to emphasize the distribution of D in euchromatin. (**g**) Classification map of nuclear regions. Segmentation based on intensity thresholds (**Supplementary Fig. 8b,c**) was used to delimitate euchromatin (red and blue regions), heterochromatin (green) and cytoplasm (gray). Additional segmentation based on a diffusion coefficient threshold at $D = 0.36$ μm^2 s^{-1} (mean + 1 s.d. of the distribution of diffusion coefficients in heterochromatin) was applied to **f** to visualize regions in euchromatin with a mean apparent diffusion coefficient of HP1α similar to the one in heterochromatin (blue regions). Scale bar, 1 μm. (**h**) ACFs calculated and averaged for the four different regions highlighted in the segmentation map (**g**). For ACF calculation in the cytoplasm, the area of the dashed rectangle in **g** was used. 2D-FCS time resolution, 700 μs.
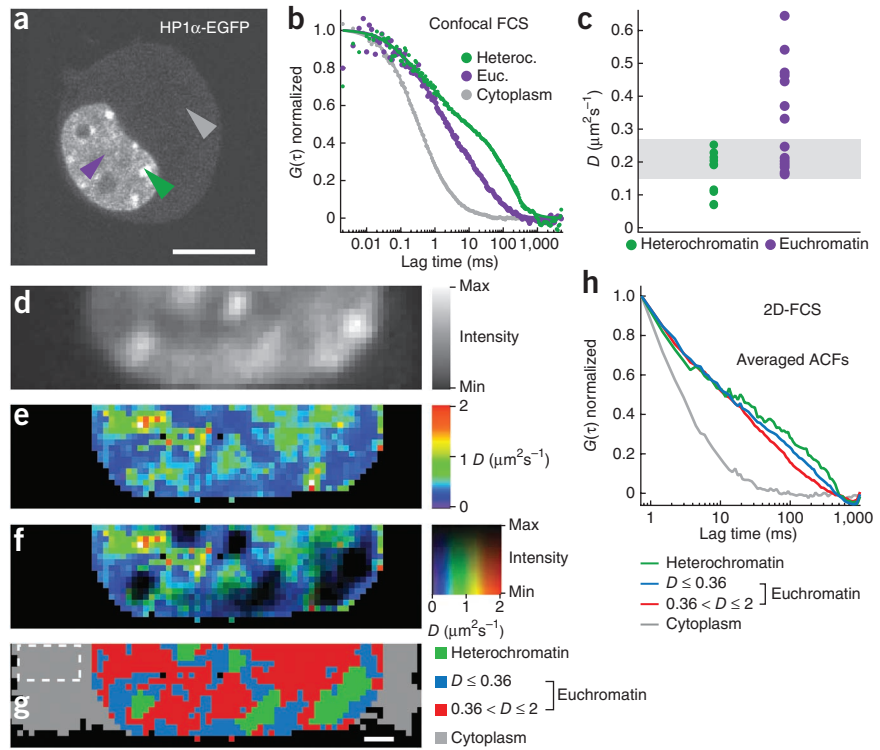
in protein mobility, for example, caused by local affinity variations. To deal with such uncertainty, the previously published values from confocal FCS for heterochromatin and euchromatin binding had to be averaged from many single-point measurements for better statistical significance[26]. However, spatially resolved information should reveal the nature of these distributions.

We used 2D-FCS to image the diffusion of HP1α in the nucleus and retrieved the free and fast-diffusing fraction of HP1α throughout the cell. A slowly diffusing fraction was observed in the entire area of the nucleus, as expected (**Fig. 4d,e** and **Supplementary Figs. 5** and **8**). The measured diffusion coefficients (0.29 ± 0.07 μm^2 s^{-1} in heterochromatin and 0.48 ± 0.25 μm^2 s^{-1} in euchromatin) were in agreement with confocal measurements (**Fig. 4c**). According to FCS theory that models the interaction, for example, of diffusible proteins with slowly mobile substrates such as chromatin[3], the value of the apparent diffusion coefficient of this slow fraction serves as a measure for the affinity of HP1α to chromatin (**Supplementary Results**). An intensity-weighted map was used to visualize low-intensity regions (euchromatin) only. This indicated a broad distribution of the values for the slowly diffusing fraction and the existence of regions in the euchromatin with heterochromatin-like affinity to HP1α (**Fig. 4f**). In the heterochromatin region, we noticed some pixels with high HP1α mobility, but too few to allow us to identify reliably a subdomain of heterochromatin.

For further analysis of the data, we used segmentation based on intensity thresholds (**Supplementary Fig. 8b,c**) to delimitate euchromatin, heterochromatin and cytoplasm. Additional segmentation based on a diffusion coefficient threshold at $D = 0.36$ μm^2 s^{-1} (mean + 1 s.d. of the distribution of diffusion coefficients in

heterochromatin) yielded extended euchromatic regions with an average diffusion coefficient of 0.29 ± 0.05 μm^2 s^{-1} (blue areas in **Fig. 4g**, average autocorrelation functions in **Fig. 4h**). They were mostly connected to heterochromatin (green areas, **Fig. 4g**) and showed the same HP1α mobility, suggesting a close relationship. The remaining regions (red areas in **Fig. 4g**) comprised ~2/3 of the euchromatin and exhibited a higher average diffusion coefficient of 0.61 ± 0.26 μm^2 s^{-1}. Notably, no correlation between HP1α signal intensity and mobility could be observed in euchromatin (compare **Fig. 4d,e**). These observations revealed that the variability of individual confocal FCS measurements of HP1α in euchromatin is likely due to a previously unresolved level of spatial organization of euchromatin into domains with low and high affinity to HP1α[23]. This demonstrates that with FCS imaging, unlike with confocal FCS, it is now possible to assign interaction and diffusion properties to every pixel of an image, providing insights into how proteins interact dynamically with cellular structures, with complete spatial coverage.

What is the nature of the extended region with higher affinity to HP1α? HP1 proteins from mammalian, *Drosophila* or the homolog Swi6 from *Schizosaccharomyces pombe* are important structural proteins of heterochromatin organization. They were proposed to be part of an epigenetic feedback loop, together with histone-modifying enzymes and histone modifications[24,27]. HP1 proteins contribute to the establishment, maintenance and spreading of heterochromatin. This applies not only to constitutive pericentric heterochromatin but also, for example, to areas of lower chromatin density, where the HP1 variants (including isoform α) participate in transcriptional repression and developmental control of local gene activity (referred to as

facultative heterochromatin[28]). In this light, our findings suggest a new level of spatial organization in the emerging differential view of HP1α as a player in gene silencing within euchromatin regions[23].

With our microscope setup, more than 6,000 FCS measurements can be performed simultaneously inside cells within a minute with an isotropic resolution of ~500 nm, providing a method to image the mobility of cellular components. This provides information that allows cellular architecture to be addressed by means of spatial maps of the mobility of the components that underlie the dynamic organization of the cell.

The introduction of light-sheet microscopy for intraorganismal live imaging[15] has triggered further developments of this platform, in particular by combining it with technologies to conduct dynamic studies[29–32]. The combination of light-sheet microscopy with FCS, as demonstrated here, provides a microscope that enables quantitative concentration, diffusion and mobility mapping by FCS imaging of fluorescent proteins with complete temporal and spatial coverage inside living cells or tissues. The arrangement of the optical system needed for high-resolution light-sheet microscopy with FCS in an upright manner enables simple sample preparation. The specimen can be placed on a coverslip in a medium-filled Petri dish that is fixed on a stage, circumventing embedding in support medium and mounting of samples as commonly used for previous SPIM setups[2]. The geometry of the setup supports a specimen of up to ~1–2 mm in diameter and is therefore compatible with studies in cells, isolated tissues and possibly even whole embryos.

Technological advances will help to further improve the performance of the FCS imaging microscope especially in terms of time resolution and readout noise of the detector arrays. The expansion of the current single-color setup to two colors is the next step toward spatial mapping of co-mobilities, namely protein-protein or protein-ligand interactions. We anticipate that these developments will become useful in the ongoing transition from conventional intensity imaging to the precise characterization of dynamic molecular processes needed for predictive modeling of cellular behavior in systems biology.

METHODS

Methods and any associated references are available in the online version of the paper at http://www.nature.com/naturebiotechnology/.

Note: Supplementary information is available on the Nature Biotechnology website.

AUTHOR CONTRIBUTIONS
M.K. and M.W. conceived the research. J.C. implemented the light-pad microscope. J.C. and M.W. conducted the yeast and mammalian work. J.C., M.W. and L.H. conducted the *Drosophila* wing disc work. J.C., M.W. and M.K. analyzed the data and wrote the manuscript. All authors commented on the manuscript.

1. Kinkhabwala, A. & Bastiaens, P.L.H. Spatial aspects of intracellular information processing. *Curr. Opin. Genet. Dev.* **20**, 31–40 (2010).
2. Huisken, J. & Stainier, D.Y.R. Selective plane illumination microscopy techniques in developmental biology. *Development* **136**, 1963–1975 (2009).
3. Elson, E.L. & Magde, D. Fluorescence correlation spectroscopy. I Conceptual basis and theory. *Biopolymers* **13**, 1–27 (1974).
4. Cheutin, T. *et al.* Maintenance of stable heterochromatin domains by dynamic HP1 binding. *Science* **299**, 721–725 (2003).
5. Bacia, K., Kim, S.A. & Schwille, P. Fluorescence cross-correlation spectroscopy in living cells. *Nat. Methods* **3**, 83–89 (2006).
6. Kim, S.A., Heinze, K.G. & Schwille, P. Fluorescence correlation spectroscopy in living cells. *Nat. Methods* **4**, 963–973 (2007).
7. Maeder, C.I. *et al.* Spatial regulation of Fus3 MAP kinase activity through a reaction-diffusion mechanism in yeast pheromone signalling. *Nat. Cell Biol.* **9**, 1319–1326 (2007).
8. Slaughter, B.D., Schwartz, J.W. & Li, R. Mapping dynamic protein interactions in MAP kinase signaling using live-cell fluorescence fluctuation spectroscopy and imaging. *Proc. Natl. Acad. Sci. USA* **104**, 20320–20325 (2007).
9. Schmidt, U. *et al.* Assembly and mobility of exon-exon junction complexes in living cells. *RNA* **15**, 862–876 (2009).
10. Kawai-Noma, S. *et al.* Dynamics of yeast prion aggregates in single living cells. *Genes Cells* **11**, 1085–1096 (2006).
11. Yu, S.R. *et al.* Fgf8 morphogen gradient forms by a source-sink mechanism with freely diffusing molecules. *Nature* **461**, 533–536 (2009).
12. Wachsmuth, M., Waldeck, W. & Langowski, J. Anomalous diffusion of fluorescent probes inside living cell nuclei investigated by spatially-resolved fluorescence correlation spectroscopy. *J. Mol. Biol.* **298**, 677–689 (2000).
13. Dertinger, T. *et al.* Two-focus fluorescence correlation spectroscopy: a new tool for accurate and absolute diffusion measurements. *ChemPhysChem* **8**, 433–443 (2007).
14. Digman, M.A. *et al.* Measuring fast dynamics in solutions and cells with a laser scanning microscope. *Biophys. J.* **89**, 1317–1327 (2005).
15. Huisken, J., Swoger, J., Del Bene, F., Wittbrodt, J. & Stelzer, E.H.K. Optical sectioning deep inside live embryos by selective plane illumination microscopy. *Science* **305**, 1007–1009 (2004).
16. Wohland, T., Shi, X., Sankaran, J. & Stelzer, E.H. Single plane illumination fluorescence correlation spectroscopy (SPIM-FCS) probes inhomogeneous three-dimensional environments. *Opt. Express* **18**, 10627–10641 (2010).
17. Kannan, B. *et al.* Spatially resolved total internal reflection fluorescence correlation microscopy using an electron multiplying charge-coupled device camera. *Anal. Chem.* **79**, 4463–4470 (2007).
18. Heuvelman, G., Erdel, F., Wachsmuth, M. & Rippe, K. Analysis of protein mobilities and interactions in living cells by multifocal fluorescence fluctuation microscopy. *Eur. Biophys. J.* **38**, 813–828 (2009).
19. Needleman, D.J., Xu, Y. & Mitchison, T.J. Pin-hole array correlation imaging: highly parallel fluorescence correlation spectroscopy. *Biophys. J.* **96**, 5050–5059 (2009).
20. Sakaue-Sawano, A. *et al.* Visualizing spatiotemporal dynamics of multicellular cell-cycle progression. *Cell* **132**, 487–498 (2008).
21. Gurdon, J.B. & Bourillot, P.Y. Morphogen gradient interpretation. *Nature* **413**, 797–803 (2001).
22. Dinant, C. & Luijsterburg, M.S. The emerging role of HP1 in the DNA damage response. *Mol. Cell Biol.* **29**, 6335–6340 (2009).
23. Kwon, S.H. & Workman, J.L. The heterochromatin protein 1 (HP1) family: put away a bias toward HP1. *Mol. Cells* **26**, 217–227 (2008).
24. Grewal, S.I. & Moazed, D. Heterochromatin and epigenetic control of gene expression. *Science* **301**, 798–802 (2003).
25. Hediger, F. & Gasser, S.M. Heterochromatin protein 1: don't judge the book by its cover! *Curr. Opin. Genet. Dev.* **16**, 143–150 (2006).
26. Müller, K.P. *et al.* Multiscale analysis of dynamics and interactions of heterochromatin protein 1 by fluorescence fluctuation microscopy. *Biophys. J.* **97**, 2876–2885 (2009).
27. Schotta, G. *et al.* A silencing pathway to induce H3–K9 and H4–K20 trimethylation at constitutive heterochromatin. *Genes Dev.* **18**, 1251–1262 (2004).
28. Grewal, S.I. & Jia, S. Heterochromatin revisited. *Nat. Rev. Genet.* **8**, 35–46 (2007).
29. Holekamp, T.F., Turaga, D. & Holy, T.E. Fast three-dimensional fluorescence imaging of activity in neural populations by objective-coupled planar illumination microscopy. *Neuron* **57**, 661–672 (2008).
30. Keller, P.J. *et al.* Fast, high-contrast imaging of animal development with scanned light-sheet-based structured-illumination microscopy. *Nat. Methods* **7**, 637–642 (2010).
31. Planchon, T.A. *et al.* Rapid three-dimensional isotropic imaging of living cells using Bessel beam plane illumination. *Nat. Methods* **8**, 417–423 (2011).
32. Ritter, J.G., Veith, R., Veenendaal, A., Siebrasse, J.P. & Kubitscheck, U. Light-sheet microscopy for single molecule tracking in living tissue. *PLoS ONE* **5**, e11639 (2010).

ONLINE METHODS

Microscope setup. The microscope is a custom-made optical setup built on a vertically erected breadboard (**Fig. 1a** and **Supplementary Fig. 1a**). The current setup is optimized for detection of GFP fluorescence. For illumination, we used the 488 nm line of an argon laser (Innova Sabre, Coherent) with an output power of 2 W. The power of the beam is first reduced using a half-wave plate (Thorlabs) combined with a Glan-Taylor polarizer (Thorlabs) and then adjusted with an acousto-optical tunable filter (AA Opto-Electronic). A single-mode optical fiber (Point Source) is used to deliver the light to the setup contained on the breadboard.

To shape the beam for the generation of the light-sheet, it is first collimated and expanded anamorphically, so that in one direction an approximately constant section of the Gaussian profile is cut out. In the other direction, the beam is focused with a cylindrical lens (f = 75.6 mm, Thorlabs). For a precise positioning of the light-sheet in the sample, the beam passes through a scanning module composed of a galvanometer-driven mirror (VM-500+, GSI) arranged at the back focal plane of an F-theta scan lens (f = 60 mm, Sill Optics). A tube lens (f = 245.60 mm, Leica) and a water dipping objective lens (Plan-Apochromat 40×/0.8 NA, Leica) with a long working distance of 3.3 mm (referred to as the illumination lens) are used to focus the light-sheet in the sample (**Supplementary Fig. 1b,c**). The width of the light-sheet can be adjusted between 20 and 200 μm by modifying the size of a slit in the x direction (**Fig. 1a**) placed in the back focal plane of the tube lens. This allows only a part of the sample to be illuminated and thus prevents photobleaching of neighboring regions during the measurement. A mirror between the scan and tube lens deflects the beam by 45° so that the objective points under 45° to a horizontal plane (bottom of the Petri dish) containing the sample.

For the collection of the emitted fluorescence, a second identical objective lens, the observation lens, is arranged in an angle of 90° to the first lens (**Supplementary Fig. 1b**). To reject reflected laser light, a dichroic mirror (AHF Analysentechnik) is placed in front of the tube lens that follows the observation lens.

Alternative detection light paths are used for intensity light-sheet imaging and FCS imaging. A mirror is used to flip the fluorescence light between the two paths. The first light path for intensity imaging includes a band-pass filter (BrightLine HC 525/45, AHF Analysentechnik) and a Keplerian telescope, which increases the total magnification to 122×. The fluorescence signal is focused onto an EM-CCD camera (QuantEM:512SC, Photometrics), referred to as the imaging camera. The pixel size of this EM-CCD in the sample plane is 131×131 nm^2 (actual size on the chip: 16×16 μm^2) and the field of view corresponds to an area of 67×67 μm^2 in the sample.

The second light path is designed for FCS imaging (1D-/2D-FCS recordings). The light passes through a band-pass filter (BrightLine HC 525/45, AHF Analysentechnik) and a scanning module (same characteristics as the illumination scanning module, see above). Spatial filtering is required to mask the unused part of the EM-CCD chip and to define the field of view. This is achieved by means of two achromatic doublets (f = 60 mm, Thorlabs) and a slit (07 SLT 701, Melles-Griot) adjustable in the y direction and placed in the image plane of the first doublet. This scanning module enables the region for FCS imaging to be positioned within the illuminated area of the sample, whereas the spatial filter allows the size of this area to be adjusted. Together with the lateral confinement of the light-sheet in the x direction by the slit in the illumination light path (see above); this allows imaging of the focal area of the light-sheet defining the light-pad (insert in **Fig. 1a** and **Supplementary Fig. 2a**). Finally, an aspherical lens (f = 40 mm, Thorlabs) focuses the fluorescent light onto a second EM-CCD camera (SamBa SE-34, Sensovation), referred to as the FCS camera. The total magnification of the second detection path is 39×, which leads to a pixel size of 190×190 nm^2 in sample space (actual size on the chip: 7.4×7.4 μm^2), and a maximum field of view that corresponds to 124×94 μm^2 in the sample plane.

The chosen vertical configuration of the setup renders possible the use of conventional Petri dishes with 60 mm diameter filled with medium into which the two objective lenses are dipped directly (**Supplementary Fig. 1b**). This avoids optical aberrations due to refractive index changes at air-glass, glass-medium or medium-agarose interfaces that can be encountered using a conventional light-sheet microscopy configuration with a dry objective lens for illumination[15]. To allow free movement of the sample,

the Petri dish is fixed on a three-axis motorized stage (stepper motors: LN-Mini23 manipulator block XY and LN-Mini Z vario, Cell Biology Trading/Luigs & Neumann) that enables positioning of the sample with an accuracy of 50 nm.

The setup is designed such that the sample can be observed from underneath, through the glass bottom of the Petri dish (Greiner bio-one, CELLSTAR 60/15 mm), with the help of a commercial inverted microscope (Olympus IX 70) equipped with a long working distance dry objective lens 20×/0.4 NA (Olympus). Due to its larger field of view, the inverted microscope allows easier and faster positioning of the light-sheet inside larger biological specimens or fast selection of cultured cells appropriate for FCS. For their observation during specimen positioning, transmitted light illumination using white light–emitting diodes placed above the Petri dish were used.

The software that controls the laser power, galvanometer-driven mirrors and stage positioning, as well as acquisition with the imaging camera, was written in LabVIEW (National Instruments). A remote control, consisting of a wireless game pad (Cordless RumblePad 2, Logitech) supported by LabVIEW, was used to control the software functions. This permits convenient control of the system during experimentation, for example, when the sample is observed through the eyepiece of the inverted microscope.

Light-pad image acquisition and processing. For light-pad microscopy using the imaging camera (light path 1, **Fig. 1a** and **Supplementary Fig. 1a**), the sample was positioned in 3D using the motorized stage. Image stacks were acquired at equidistant sample positions along the optical axis of detection (z axis) for the case of roundish objects (such as beads or yeast cells). For the case of laterally extended objects such as *Drosophila* wing imaginal discs, stacks of images were acquired horizontally (in y-z direction). Larger effective fields of views (**Fig. 3a** and **Supplementary Video 5**) were achieved by tiled imaging of neighboring regions and by increasing the focal length of the light-sheet by reducing the back aperture size of the illumination objective lens. ImageJ (US National Institutes of Health) was used to shear the horizontally acquired image stacks to transform them into conventional z-stacks and to apply linear contrast adjustments.

FCS imaging data acquisition. For 1D-FCS data acquisition, light path 2 leading to the FCS camera was used (**Fig. 1a** and **Supplementary Fig. 1a**). To increase the time resolution, the EM-CCD was operated in line-scan mode as described previously[33,34]. Instead of transferring a complete frame from the sensor area to the storage area of the chip between subsequent exposure intervals, only a single line was shifted. Then, a fraction of a complete line was transferred through the A/D conversion and amplification chain of the chip and to the framegrabber card PCI-1422 (National Instruments). The readout process is the time-limiting step of CCD image acquisition and this procedure increased considerably the time resolution, for example, leading to 40 μs (or 25,000 lines per second) for a fraction of 120 pixels of a line. For *in vivo* measurements, we usually acquired 340 pixels (half a line) to extend the field of view with a time resolution of 70 μs. To increase the number of photoelectrons per data point, we arranged the spatial filter in the detection path such that three lines were illuminated as adapted to the size of the PSF on the chip (**Supplementary Results**) and applied lateral 3-pixel binning to the raw data before further processing.

2D-FCS measurements were carried out following the same procedure as for 1D-FCS. However, the size of the spatial filter (light path 2) was adjusted to illuminate 20 lines of the EM-CCD chip. Also, 20 lines were transferred to the storage area between subsequent exposure intervals and then converted, amplified and transferred to the framegrabber as a single frame. Here a time resolution of 700 μs could be achieved when using a frame size of 20 lines of 340 pixels.

We acquired the fluorescence signal in all measurements for periods of ~30–60 s. The laser was switched off for the first 5 s to assess the overall background of the measurement. Raw data were saved as multilayer tiff files to the hard disc of the PC. Image data acquisition with the FCS camera was carried out with self-written software in Visual C++.

The laser power used for FCS imaging was measured at the focal plane of the illumination lens using a Nova II power meter equipped with a PD300 detector (Ophir Optronics, Jerusalem, Israel). In a typical 1D-/2D-FCS *in vivo* experiment, the illumination laser power measured in the focus of the light-sheet

was about 700 µW. Considering the light-sheet cross-section as a rectangle of 65 µm (typical light-sheet width used for FCS) by 700 nm (light-sheet thickness; **Supplementary Fig. 2c,d**) yields an intensity of ~1.5 kW cm^{-2}. This corresponds to the focal intensity in a confocal FCS setup with an 1.2 NA water objective lens, a focal radius of 240 nm and a focal laser power of 2.8 µW, that is, at the lower limit of the intensities typically used for confocal FCS measurements[35]. Thus, the intensity used in a confocal setup to conduct one FCS measurement allowed us to conduct 20 measurements (along the 20 pixels) and prevented at the same time out-of-focus illumination. The light-pad microscope provides therefore an at-least 20-fold increased efficiency as compared to a confocal FCS setup.

Confocal image and FCS data acquisition. Confocal fluorescence images, image stacks and FCS data were acquired on an inverted Leica confocal laser scanning microscope TCS SP5 AOBS SMD FCS equipped with an HCX PlanApo CS 63×/1.2 NA water immersion objective lens (Leica). For excitation, the 488 nm line of an argon laser was used. The fluorescence was detected with a photomultiplier tube for imaging and an SPCM-AQR-14 avalanche photodiode (PerkinElmer Optoelectronics) for FCS with the spectral detection window set to 500–550 nm. The diameter of the detection pinhole was fixed to 1 Airy disc. The laser power in the sample was well below 200 µW for FCS and below 500 µW for confocal laser scanning microscopy acquisition as measured in front of the objective lens using the Nova II power meter. For FCS data acquisition, the beam was parked at a position of interest in a previously acquired image, and laser illumination and detector read-out were started for 30–60 s. Data were acquired using the PicoQuant SymPhoTime software of the microscope and stored in binary raw format.

FCS data processing and analysis. For each pixel of every 1D- and 2D-FCS recording, the intensity time trace $F_{x,y}(t)$ from pixel x in line y could be extracted from the image files after subtracting the background signal as acquired in the first 5 s and after transforming the pixel gray values into numbers of photoelectrons as described previously[18,33]. From the resulting fluorescence intensity traces as well as from the confocal FCS measurements, the autocorrelation (ACF; $x_1 = x_2 \wedge y_1 = y_2$) and cross-correlation (CCF; $x_1 \neq x_2 \vee y_1 \neq y_2$) functions were computed using the Fluctuation Analyzer software written in our laboratory in Visual C++ according to

$$G_{x_1,y_1,x_2,y_2}(\tau) = \frac{1}{T}\int_0^T dt'\, G_{x_1,y_1,x_2,y_2}(t',\tau),$$

$$G_{x_1,y_1,x_2,y_2}(t',\tau) = \frac{\left\langle \delta F_{x_1,y_1}(t)\delta F_{x_2,y_2}(t+\tau) + \delta F_{x_2,y_2}(t)\delta F_{x_1,y_1}(t+\tau)\right\rangle_{t',T_{\text{win}}}}{2\left\langle F_{x_1,y_1}(t)\right\rangle_{t',T_{\text{win}}}\left\langle F_{x_2,y_2}(t)\right\rangle_{t',T_{\text{win}}}},\quad(1)$$

$$\delta F_{x,y}(t) = F_{x,y}(t) - \left\langle F_{x,y}(t)\right\rangle,\ \langle\ldots\rangle = \frac{1}{T}\int_0^T dt\ldots.$$

This included a sliding average approach to correct for slow signal variations, for example, due to photobleaching. The correlation functions were calculated for all possible segments of length T_{win} of 1–2 s and then averaged over the complete acquisition time T. This will be described in more detail elsewhere.

The resulting ACFs and CCFs were fitted in Matlab (The MathWorks) using the nonlinear least-squares Levenberg-Marquardt algorithm with the general model function[36]

$$G_{x_1,y_1,x_2,y_2}(\tau) = \frac{1}{N}\left[1-\Theta+\Theta\exp\left(-\frac{\tau}{\tau_{\text{blink}}}\right)\right]$$
$$\sum_{i=1}^{2} f_i\left[1+\left(\frac{\tau}{\tau_{\text{diff},i}}\right)^{\alpha_i}\right]^{-1}\left[1+\frac{w_0^2}{z_0^2}\left(\frac{\tau}{\tau_{\text{diff},i}}\right)^{\alpha_i}\right]^{-1/2}$$
$$\times\exp\left\{-\frac{(x_2-x_1)^2\delta^2+(y_2-y_1)^2\delta^2}{w_0^2}\left[1+\left(\frac{\tau}{\tau_{\text{diff},i}}\right)^{\alpha_i}\right]^{-1}\right\}, (2)$$

in which N is the (apparent) number of molecules and which accounts for molecular blinking with the fraction Θ of molecules in a nonfluorescent state of

lifetime τ_{blink} and considering anomalous diffusion of two components $f_1, f_2 = 1-f_1$ with the diffusion correlation times $\tau_{\text{diff},i} = w_0^2/(4D_i)$, the lateral and the axial focal radii w_0, z_0 and the focal volume $V = \pi^{3/2}w_0^2z_0$, the apparent diffusion coefficients D_i as well as the anomaly parameters α_i of components $i = 1,2$. In the case of CCFs, the pixel displacement was taken into consideration with the second exponential term including the pixel size δ and the pixel indices x_1, y_1, x_2, y_2, whereas for ACFs, that term was 1. The radii w_0, z_0 were set to the values obtained from the PSF measurements (**Supplementary Results**). For 1D- and 2D-FCS data of fluorescent beads and Alexa488, curve fitting was done without any blinking contribution, that is, $\Theta = 0$. For confocal and 1D-FCS data of green fluorescent proteins, the nonfluorescent lifetime was set to 100 µs[12]. For 2D-FCS data, the time resolution of 0.7 ms allowed us to neglect the blinking contribution, i.e., $\Theta = 0$. Thus, for a single-component fit, we set $f_1 = 1$, resulting in the three free fit parameters N, $\tau_{\text{diff},1}$, α_1 for 2D- and the additional parameter Θ for 1D-FCS. Two-component fitting required the additional free parameters f_1, $\tau_{\text{diff},2}$, α_2. The goodness of the fit was assessed by means of the R-square value (R_{adj}^2) adjusted to the degrees of freedom with $0 \leq R_{\text{adj}}^2 \leq 1$. In general, we accepted any fit with $R_{\text{adj}}^2 \geq 0.8$.

In this way, profiles (1D-FCS) or maps (2D-FCS) of the fit parameters, of the goodness of fit R_{adj}^2 and of the pixel intensity were created (**Supplementary Fig. 8**). By applying a threshold to the intensity and/or R_{adj}^2 maps, we generated binary masks to exclude noisy data and/or any unsatisfactory fit and to pick those regions, for which the finally resulting concentrations, diffusion coefficients and fractions of components were mapped.

We noticed that the slower acquisition speed associated with 2D-FCS recordings affected mostly the precision with which the concentration could be estimated. We computed simulated autocorrelation functions according to equation (2) including Gaussian noise for an amplitude of 1 and a diffusion correlation (or dwell) time of 3 ms (as expected and observed for GFP *in vivo* in our setup) with time resolutions (or shortest lag times) of 1, 40, 700 and 1,400 µs. Fitting the ACFs with equation (2) yielded virtually the same amplitude, however, the corresponding confidence interval increased 1.5-, three- and fivefold, respectively. Likewise, the diffusion correlation time retrieved from the fit was almost independent of the time resolution, and even the corresponding confidence interval remained nearly unaffected. Thus, we consider the fit results for diffusion properties and concentrations as correct and reliable even for free diffusion of fluorescent proteins *in vivo* measured with 2D-FCS. Nevertheless, the accuracy of protein concentration measurements is expected to improve further by a better time resolution of the 2D-FCS acquisition using the next generation of detector arrays.

Sample preparation. The PSF measurements were carried out by acquisition of image stacks of 20-nm-diameter fluorescent beads with an excitation maximum at 505 nm and an emission maximum at 515 nm (yellow-green carboxylate-modified FluoSpheres, Molecular Probes). Before imaging, the beads were sonicated and embedded in 1% low-melting agarose at a concentration of ~5 nM. For light-pad imaging, the solidified agarose gel was placed in the center of a 60 mm diameter Petri dish containing distilled water. Isolated beads at the water-agarose interface were chosen. For confocal imaging, the gel was placed in an 8-well chambered cover glass (Nunc). Isolated beads close to the glass-agarose interface were chosen.

For *in vitro* FCS measurements solutions of the same beads in water or Alexa488 (Molecular Probes) dissolved at a concentration of 250 nM either in water, in 1× PBS buffer or in 1× PBS buffer supplemented with Ca^{2+} (0.9 mM) and Mg^{2+} (0.5 mM) were used. The solutions (~0.35 ml) were each placed in the center of a Petri dish between the two objectives of the light-pad microscope.

Replication-defective, self-inactivating lentivirus vectors were used to produce clonal MDCK cell lines stably expressing the Fucci cell cycle marker[20]. Lentiviral vectors CSII-EF-mKO2-hCdt1 and CSII-EF-mAG-hGem were obtained from the Riken BioResource Center, Japan. The plasmids were cotransfected with the packaging vector (pCMV-dR8.2 dvpr, Addgene plasmid 8455) and the envelope vector (pCMV-VSV-G, Addgene plasmid 8454) into 293T cells. Cells were cultured in MEM supplemented with penicillin-streptomycin and 5% FBS at 37 °C and 5% CO$_2$. For light-pad imaging and FCS recordings, cells were grown on pieces of 1-mm thick cover slide glass of ~4 × 10 mm^2, which were transferred to Petri dishes (60 mm diameter) containing 1× PBS before the experiments.

3T3 cells stably expressing HP1α-EGFP were cultivated, as described previously[26]. For confocal imaging and FCS measurements, cells were grown in 8-well chambered cover glasses (Nunc) and the medium was replaced by phenol red–free medium before the experiments. For light-pad imaging and FCS measurements, cells were grown on pieces of 1 mm thick cover slide glass of ~4 × 10 mm², which were transferred to Petri dishes containing 1× PBS before the experiments.

D. melanogaster wing imaginal discs were isolated from late third-instar larvae. Larvae were dissected in 1× PBS buffer supplemented with Ca²⁺ (0.9 mM) and Mg²⁺ (0.5 mM) or in Express Five SFM (Gibco). Discs were mounted with the peripodial membrane down in a drop of 0.5–1% methyl cellulose (Sigma) in PBS/Ca²⁺ + Mg²⁺ on a 1 mm thick coverslide glass of ~4 × 10 mm². Within 5–10 min after mounting, FCS and intensity imaging were performed at various positions in the wing pouch.

Yeast cells expressing the protein Pma1 tagged with GFP from the endogenous chromosomal location[37] were used. Cells were grown in synthetic complete yeast medium and adhered to the surface of a rectangular piece of glass (~4 × 10 mm²) by Concanavalin A treatment as described before[7]. For light-pad imaging the glass piece was placed in the center of the Petri dish containing synthetic complete yeast medium.

33. Bestvater, F. *et al.* EMCCD-based spectrally resolved fluorescence correlation spectroscopy. *Opt. Express* **18**, 23818–23828 (2010).
34. Im, K.B. *et al.* Two-photon spectral imaging with high temporal and spectral resolution. *Opt. Express* **18**, 26905–26914 (2010).
35. Gregor, I., Patra, D. & Enderlein, J. Optical saturation in fluorescence correlation spectroscopy under continuous-wave and pulsed excitation. *ChemPhysChem* **6**, 164–170 (2005).
36. Gröner, N., Capoulade, J., Cremer, C. & Wachsmuth, M. Measuring and imaging diffusion with multiple scan speed image correlation spectroscopy. *Opt. Express* **18**, 21225–21237 (2010).
37. Huh, W.K. *et al.* Global analysis of protein localization in budding yeast. *Nature* **425**, 686–691 (2003).